Ceramics International 43 (2017) 1543–1551

Contents lists available at ScienceDirect

Ceramics International

journal homepage: www.elsevier.com/locate/ceramint

High-temperature antiferroelectric and ferroelectric phase transitions in phase pure $LaTaO_4$

Yuslín G. Abreu[a,b], Kisla P.F. Siqueira[a], Franklin M. Matinaga[c], Roberto L. Moreira[c], Anderson Dias[a,*]

[a] Departamento de Química, Universidade Federal de Ouro Preto, Campus Morro do Cruzeiro, ICEB II, Ouro Preto, MG 35400-000, Brazil
[b] Facultad de Física-Instituto de Ciencia y Tecnología de Materiales, Universidad de La Habana, San Lázaro y L, Vedado, La Habana 10400, Cuba
[c] Departamento de Física, ICEx, Universidade Federal de Minas Gerais, C.P. 702, Belo Horizonte, MG 30123-970, Brazil

ARTICLE INFO

Keywords:
Ferroelectrics
$LaTaO_4$
Vibrational spectroscopy
Dielectrics
Phase transitions

ABSTRACT

Phase-pure $LaTaO_4$ ceramics was prepared by solid-state reaction. Dielectric spectroscopic data as well as differential scanning calorimetric experiments showed the existence of a sequence two high-temperature first-order structural phase transitions. The first phase transition occurs above 160 °C (on heating), from the monoclinic $P21/c$ space group at room temperature to the polar orthorhombic $Cmc2_1$ group, exhibiting a very large thermal hysteresis probably linked to the reconstructive nature of the structural transition. The second transition occurs around 225 °C to the orthorhombic Cmcm space group, with a small thermal hysteresis. Vibrational Raman spectroscopic analyses confirmed these two sequential phase transitions, as well as the thermal hysteresis observed for both first-order transitions in repeated heating and cooling cycles. The existence of a strong monoclinic distortion at room temperature could be related to the presence of defects (oxygen vacancies) in $LaTaO_4$ ceramics, after sintering. Dielectric spectroscopy showed a strong influence of the electric conductivity on the dielectric response with activation energy of *dc* component of conductivity (0.62 eV) compatible with the presence of oxygen vacancies. Far-infrared data confirmed that the extra modes observed in the Raman spectra are forbidden bands, which were activated by defects into the structure.

1. Introduction

Lanthanide orthotantalate compounds are members of the ABO_4 family studied for their photocatalytic and electronic activities, ionic conductivity and luminescence properties [1–6]. Proton conductivity has been observed in some lanthanide orthotantalate materials as a consequence of their crystal symmetry at low and high temperatures [1]. In this family, $LaTaO_4$ ceramics are recognized for their polymorphic forms, which are related to the preparation routes employed [7–11]. In the point of view of their crystal structures, Cava and Roth [7] reported a non-centrosymmetric space group ($Cmc2_1$) at 300 °C, whereas the symmetry at room temperature would be monoclinic (space group $P21/c$). The existence of thermal hysteresis between the phase transition (PT) temperatures was observed by these authors from X-ray diffraction data upon heating and cooling runs (175/150 °C).[7] The relationship between the crystal symmetries at high and low temperatures was interpreted by the changes in both shape or dimension of the TaO_6 octahedra. Cava and Roth [7] listed the main changes as the small increase in the height of the octahedra in the *c*-direction, the difference in the Ta-O bond distances, and the change in the coordination of the lanthanum ions due to the reorientation of the TaO_6 octahedra. The analogy between $LaTaO_4$ and the isostructural $BaMnF_4$ compound was established by Cava and Roth [7] and by Scott [11], concerning also the high-temperature structural sequence. Additionally, $BaMnF_4$ is characterized by a commensurate-incommensurate PT at low temperatures, and exhibits planar structures and magnetoelectric effects (geometrical ferroelectrics). The main difference between these compounds is in the coordination of the Ba/La atoms along the *b*-axis, being associated with the way in which these ions bond neighboring sheets of MnF_6/TaO_6 octahedra. Lanthanum is coordinated with two oxygen ions, whereas the Ba is coordinated with one fluorine ion [7].

The existence of a monoclinic to orthorhombic PT in $LaTaO_4$ was also found by Vullum et al. [12] by using differential scanning calorimetry. The PT was observed around 240 °C, upon heating and 5 °C below this temperature during cooling. The polymorphism exhibited by this sample was considered as a consequence of the annealing temperatures and pressures applied during the sample

* Corresponding author.
E-mail address: anderson_dias@iceb.ufop.br (A. Dias).

http://dx.doi.org/10.1016/j.ceramint.2016.10.128
Received 9 September 2016; Received in revised form 15 October 2016; Accepted 20 October 2016
Available online 24 October 2016

preparation. Recently, a more detailed structural investigation was conducted in the system $La_{1-x}Nd_xTaO_4$ ($0 \le x \le 0.6$) [9]. The results showed a noncentrosymmetric orthorhombic phase ($Cmc2_1$) at room temperature for pure $LaTaO_4$ (x=0) and a centrosymmetric monoclinic phase ($P21/c$) for the Nd-doped samples [9]. The thermal evolution of the dielectric permittivity showed, for pure $LaTaO_4$, a ferroelectric (FE)–paraelectric (PE) PT around 200 °C, in correspondence with the structural transition observed by XRD towards the orthorhombic centrosymmetric Cmcm space group. However, the doped samples revealed the existence of two peaks in the temperature dependence of the dielectric permittivity. The first one was related to a first-order antiferroelectric (AFE)–FE transition in the region 250 °C < T < 350 °C. The second peak in the dielectric permittivity was observed at 400 °C and was attributed to an orthorhombic (FE)–orthorhombic (PE) PT. Phase transitions for Nd-doped samples were then explained by the authors from high temperature data, in which the higher temperature (more symmetric) orthorhombic structure without octahedra tilting changes to another orthorhombic phase (lower temperature) with in-phase octahedra tilting about the a-axis [9]. This in-phase tilting produces an increase of the polar c-axis and lead to the presence of an orthorhombic $Cmc2_1$ structure. Finally, anti-phase tilting around c-axis accompanying the FE-PE transition, results in a centrosymmetric structure $P21/c$. From the discussion made by Cordrey et al. [9], the presence of Nd^{3+} into the structure would stabilize the monoclinic phase at room temperature. However, the association between the monoclinic $P21/c$ distortion and the presence of Nd^{3+} in the $LaTaO_4$ system is not well understood, because previous studies reported the existence of this monoclinic distortion even for pure $LaTaO_4$ ceramics [7,8,12,13]. Also, Siqueira et al. [8] showed previously that $LaTaO_4$ and $NdTaO_4$ present different structures, Nd-based ceramics exhibiting a fergusonite M-type structure, I2/a (C_{2h}^6, #15, Z=4). This fact was not considered by Cordrey et al. [9] in their assumptions, although the competition between these structures could help to understand their results. In this sense, this work presents a new detailed structural investigation in phase-pure $LaTaO_4$ ceramics as a function of temperature. Dielectric spectroscopy was employed in a wide range of frequency and temperature; besides, differential scanning calorimetry, Raman scattering and infrared spectroscopy were used to investigate the sequence of structural PT. A very large thermal hysteresis was confirmed for the AFE-FE PT and is discussed in terms of the reconstructive nature of this transition and the presence of oxygen vacancies in the sintered phase pure $LaTaO_4$ ceramics. On the other hand, the FE-PE PT showed a very small first-order character, as showed by the small thermal hysteresis and faint entropy jump at the critical temperature.

2. Experimental

$LaTaO_4$ ceramics were synthesized by using La_2O_3 and Ta_2O_5 (> 99.9% Sigma-Aldrich) as starting materials through solid-state reaction. Stoichiometric amounts were weighed and mixed with a mortar and pestle. The mixed powders were calcined at 1300 °C for 14 h. For sintering, cylindrical pucks of about 5 mm height and 12.5 mm diameter were made by applying a pressure of 150 MPa. The samples were then sintered in a conventional oven at 1500 °C, for 4 h. The final density of the samples was calculated as 97.5% of the theoretical value by using the Arquimedes method. All samples were characterized by X-ray diffraction (XRD) using a Shimadzu D-6000 diffractometer with graphite monochromator and a nickel filter in the range of 10–60°2θ (15 s/step of 0.02°2θ), operating with FeKα radiation (λ=0.1936 nm), 40 kV and 20 mA (the results were automatically converted to CuKα radiation for data treatment and manipulation). The software MDI Jade 9.0 was employed to calculate the lattice parameters of the ceramic samples.

For the dielectric measurements, electrodes were made by Ag paste on the parallel surfaces of the previously polished samples. I-V characteristic curves confirm the ohmic nature of these contacts. Four-point *ac* impedance measurements (500–1 MHz, applied signal of 200 mV) were performed between room temperature and 500 °C, using an Impedance Analyzer HP4192A, in a parallel (capacitance, conductance) circuit mode. Conventional (1 m length) coaxial cable connected the equipment with a cold extremity of an alumina sample holder. Shielded gold wires of 20 cm make the contact with the sample, placed in the other extremity of the holder. The heating/cooling rates employed were 2 °C/min, under nitrogen atmosphere. The experimental setups employed allowed us to measure dielectric data up to 1 MHz with very low fractional errors. Differential scanning calorimetry (DSC) was carried out by using a Q2000 equipment from TA Instruments. The sample (30.51 mg) was analyzed under helium gas flow of 50 mL/min. We adopted the following DSC protocol: heating rate of 5 °C/min from −20 to 320 °C, cooling with the same rate to −20 °C.

Fourier-transform infrared reflectivity was performed in a Nicolet Nexus 470 equipment, with a Centaurus microscope (10×magnification, incident light beam with 350 μm diameter). In its commercial configuration, designed only for mid-infrared measurements (550–4000 cm^{-1}), this spectrometer uses a SiC source, a KBr: Ge beamsplitter and a liquid N_2 cooled HgCdTe (MCT) detector. Mid-infrared reflectivity spectra were obtained under nitrogen purge, by averaging 128 scans, using observation regions of 250 μm×250 μm, with spectral resolution of 2 cm^{-1}. Gold mirrors were used for the reference spectra. The samples were previously polished to an optical grade. The sample surfaces were plane and smooth enough in many regions within the observation area to give quite appropriate spectra. Far-infrared measurements were carried out in a Centaurus microscope adapted according to procedures described previously [14,15]. Vibrational data (50–700 cm^{-1}) were collected using a Si-beamsplitter and a Si-bolometer detector, by averaging 128 scans. All other experimental conditions were the same as used for mid-infrared measurements. The reflectivity spectra obtained in mid- and far-infrared regions matched well in the superposition region. The overall spectra (50–4000 cm^{-1}) were treated within the four-parameter semi-quantum oscillator model.

Raman spectra of either as-synthesized and sintered samples at room temperature were collected in backscattering configuration by using an Horiba/Jobin-Yvon LABRAM-HR spectrometer with the 632.8 nm line of a helium-neon laser (effective power of 6 MW at the surface of the sample) as excitation source, diffraction gratings of 600 and 1800 grooves/mm, Peltier-cooled CCD detector, confocal Olympus microscope (100×objective), and experimental resolution typically 1 cm^{-1} for 10 accumulations of 30 s. Appropriate interference filter for rejecting laser plasma lines, edge filter for stray light rejection were used. For high-temperature measurements (from RT to 300 °C), it was employed a Jobin-Yvon T64000 triple-monochromator equipped with a LN_2-cooled CCD detector and an Olympus microscope (20×objective). The measurements were carried out in backscattering geometry, using the 532 nm line of a Coherent-Verdi laser (doubled frequency of a YVO_4:Nd laser, 10 MW at the surface of the $LaTaO_4$ ceramics) as excitation source. The spectral resolution was better than 2 cm^{-1} and the accumulation times were typically 10 collections of 60 s. $LaTaO_4$ samples were mounted in a temperature controlled (accuracy of about 0.1 K) heating stage (Linkam), which was placed under the microscope's objective for the high-temperature measurements. All resulting spectra were corrected by the Bose-Einstein thermal factor.

3. Results and discussion

Fig. 1 presents the XRD pattern for the $LaTaO_4$ ceramics studied in this work. XRD data were indexed according to the International Committee for Diffraction Data (ICDD) card #72–1808. Single-phase, crystalline ceramics were obtained after sintering without contaminants or secondary phases. $LaTaO_4$ ceramics crystallized within the monoclinic structure, $P21/c$ space group (C_{2h}^5, #14 and Z =4), with

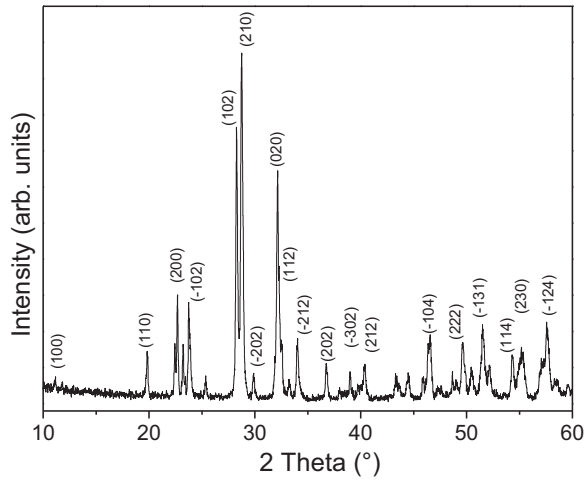

Fig. 1. Room-temperature XRD pattern for the sintered $LaTaO_4$ sample with the respective crystallographic planes, indexed after the ICDD card #72–1808.

lattice parameters a =7.701 Å b =5.561 Å c =8.122 Å and β=103.7° (obtained from software MDI Jade version 9.0) This structure was firstly described by Cava and Roth [7] and is formed by noncoplanar arrays of oxygen ions with 8-fold coordinated tantalum ions. It was observed that the β angle, which characterize the monoclinic distortion of the sample, showed higher values than those previously reported for pure and doped $LaTaO_4$ ceramics [7,9].

The temperature dependence of the real part of the dielectric permittivity of $LaTaO_4$ ceramic (ε') is shown at selected frequencies in Fig. 2, upon heating and cooling. As it can be seen, two major occurrences are easily visualized in the experimental curves. The first one is an abrupt increase in ε′ observed around 160 °C upon heating, and the corresponding abrupt decrease in ε′ at around 37 °C upon cooling. The second occurrence is a peak observed around 225 °C upon heating, and around 220 °C upon cooling. The difference in temperature for the occurrence of the first event upon heating and cooling runs shows the existence of a very large thermal hysteresis in our $LaTaO_4$ ceramics. It can be observed that the temperature, which corresponds with the maximum for ε′, is independent of the frequency for all events. The real dielectric permittivity showed an abrupt increase from 300 °C, which is more visible at lower frequencies, suggesting a strong influence of the electric conductivity in the properties of the studied sample. The presence of two events in ε′ could suggest the existence of two phase transitions for the $LaTaO_4$. In a previous work, Cava and Roth [7] investigated the structural transitions for the same material

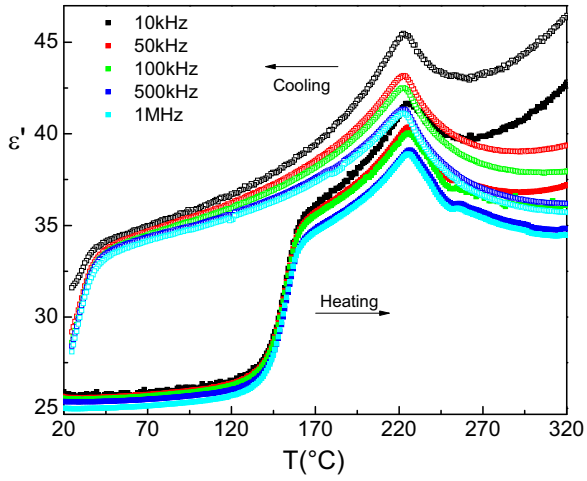

Fig. 2. Temperature dependence of the real dielectric permittivity ε′ of $LaTaO_4$ ceramic at selected frequencies.

and observed a temperature transition value for the AFE-FE transitions 15 °C above to that observed in ε′ for the first phase transition upon heating (around 175 °C). These authors did not observe the higher temperature ferroelectric transition.

A previous dielectric study [9] for phase-pure $LaTaO_4$ showed also only one phase transition, but that associated with a second-order FE–PE transition: from the polar orthorhombic $Cmc2_1$ phase to the non-polar orthorhombic Cmcm phase. However, for the Nd-doped $La_{1-x}Nd_xTaO_4$ system, the same authors verified two transitions in the temperature dependence of ε′. The first transition showed a marked hysteresis, indicating the first-order character of the AFE-FE phase transition for the Nd-doped sample. This behavior was related with the structural transition from non-polar monoclinic ($P21/c$) phase to polar orthorhombic ($Cmc2_1$) phase. The second transition would present the same nature than that for their undoped $LaTaO_4$ samples. The existence of a monoclinic phase at room temperature was attributed by Cordrey et al. [9] to the small amount of Nd doping into the La site. The distortion of the structure is considered as a consequence of the presence of smaller Nd ions. In our case, the two anomalies verified in the temperature dependence for the real dielectric permittivity could be associated with the existence of a sequence of AFE-FE-PE phase transitions, as also observed by Cordrey et al. [9] in Nd-doped $LaTaO_4$. Indeed, Siqueira et al. [8] have investigated lanthanide orthotantalates and verified that Nd-based orthotantalates belong to a different monoclinic structure than that observed for $LaTaO_4$. Since La and Nd ions present the same oxidation state, the changes in the transition temperatures would be the consequence of steric changes (elastic distortions) due to the different ionic sizes and to the competition between La and Nd for different structures.

Fig. 3a shows the temperature dependence of the imaginary part of the dielectric permittivity (ε″) upon cooling at several frequencies. Fig. 3b shows the dependency of the *ac* conductivity with the reciprocal temperature, also on cooling runs. The abrupt increase of ε″, more visible at lower frequencies, is in correspondence with the noticeable increase of ε′ at higher temperatures and lower frequencies. This behavior supports the strong influence of the electrical conductivity in the dielectric response of the studied sample. The influence of the conductivity hinders the observation of any peak associated with the transitions observed in ε″. However, the inset in Fig. 3a shows, for higher frequencies, a weak peak around 225 °C. This peak is observed at the same temperature for all the frequencies, and corresponds with the temperature of the second peak observed in ε′ on cooling (FE-PE transition).

For the *ac* conductivity curve above 440 °C (Fig. 3b), the presence of the *dc* component for the total conductivity was observed at lower frequencies. A change in the slope of the conductivity is observed around 225 °C, where the real and imaginary parts of the dielectric permittivity showed a peak in its dependency with temperature. The change in slope must be related with the FE-PE phase transition. The plot region of the lower frequencies was used to estimate the activation energy for the *dc* conductivity at higher temperature range. The obtained value was found to be 0.62 eV, which is typically associated with the presence of oxygen vacancies [16,17]. These point defects (oxygen vacancies) with single and/or double ionization could be present in $LaTaO_4$ studied here, and probably come from the preparation process. These vacancies exhibit low mobility at room temperature, and increase their mobility with the increase in the temperature, being activated and contributing with the total electrical conductivity. The presence of single and double ionized oxygen vacancies in $LaTaO_4$ ceramics have been previously detected from photoluminescence measurements [18]. The presence of oxygen vacancies in the studied sample has an important influence in the structure stability, as will be discussed below.

DSC data are presented as thermograms in Fig. 4 for the $LaTaO_4$ ceramic investigated. The presence of two reversible enthalpic anomalies at about 160 °C and 240 °C is clearly seen on heating (black curve),

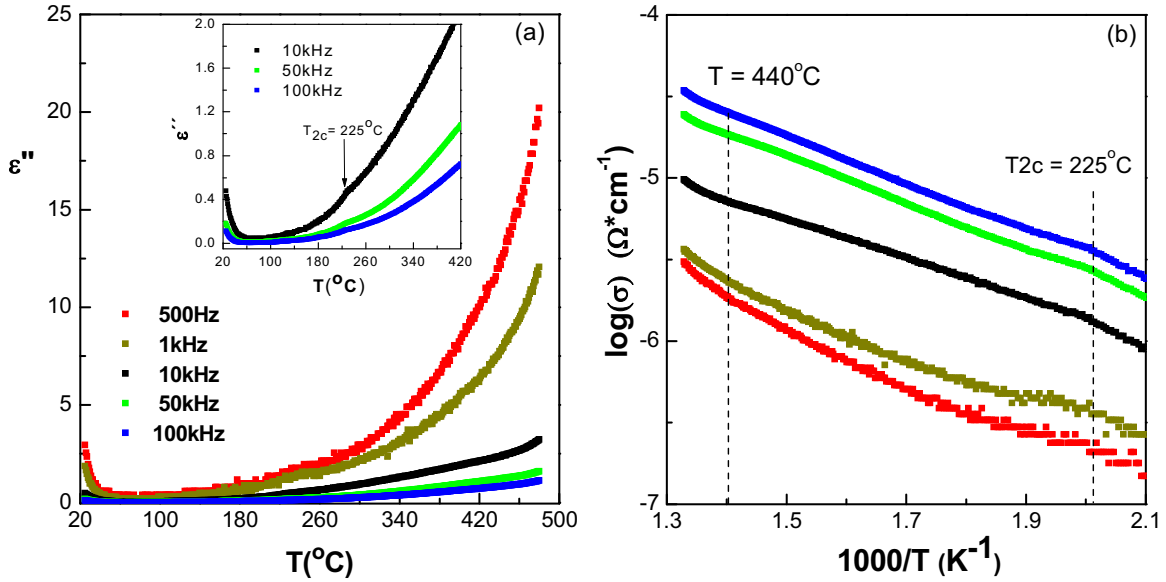

Fig. 3. Temperature dependence on cooling for (a) the imaginary dielectric permittivity and (b) the *ac* conductivity at 0.5, 1, 10, 50, and 100 kHz. The inset in (a) shows the imaginary part of the dielectric permittivity at 10, 50 and 100 kHz, for better visualization.

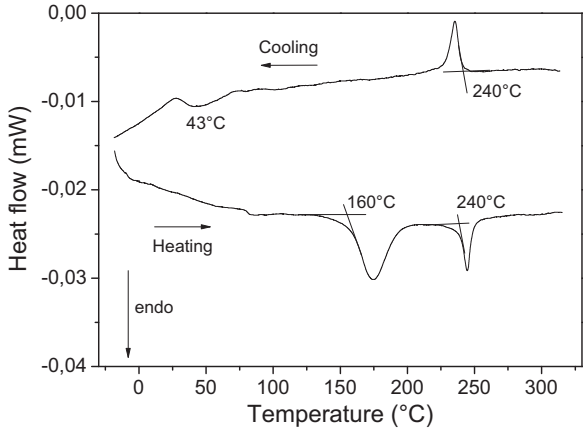

Fig. 4. DSC thermograms for the $LaTaO_4$ ceramics, showing the two structural phase transitions, both with first-order character.

taken on the onset of the peaks. As it can be seen, both anomalies indicate first-order phase transitions, the first one with a very large thermal hysteresis (160 °C/43 °C). Nevertheless, within the experimental accuracy of our apparatus (1 °C), we have not discerned thermal hysteresis in the second phase transition (around 240 °C), although the reversible character and the corresponding latent heat confirm its first-order nature. As a whole, these results are in good agreement with the dielectric spectroscopic data, discussed above. The energies evolved during transitions were determined from the DSC thermograms as 25.6 J/mol and 7.9 J/mol for the first and second phase transitions, respectively. From these enthalpies, it was possible to calculate the entropy-jumps for these transitions as 0.050 and 0.018 J/K mol, which correspond to typical entropies for displacive-type phase transitions. It is worthy noticing that the PT are smeared, revealing an important influence of charged defects on the stabilization of the AFE and the FE phases (charged defects ca lock the octahedral tinting, increasing the critical temperatures). This is particularly more important for the AFE-FE transition, due to its reconstructive nature, where the octahedral tinting changes from the A-axis to the c-axis. In this case, charged defects can lock one or another octahedral tinting, increasing the thermal hysteresis.

Raman spectra for the $LaTaO_4$ ceramics upon heating are shown in Fig. 5, in the temperature range 26–300 °C. The spectra showed remarkable changes with the temperature. The number of active modes observed in the studied samples showed a tendency to decrease for increasing temperatures. Three different colors were used in Fig. 5 to show the temperature ranges where the noticeable changes occur, typically the decreasing of the number of active modes, associated with structural phase transitions undergone by the sample. The first range between 26 and 140 °C is represented in black, while the second range (160–220 °C) is shown in blue. The third temperature range occurs for 240–300 °C and is represented by red curves. The modes marked with numbers are present in the three structures of the $LaTaO_4$ ceramics. The first significant change on the Raman spectra (Fig. 5) occurs between 140 °C and 160 °C and coincides with the noticeable increase in the real part of the dielectric permittivity with temperature upon heating. Thus, Raman spectra corroborate the structural PT above 160 °C. The second important change was observed in the Raman spectra between 220 °C and 240 °C. Similarly, the real dielectric permittivity presented a second peak at 225 °C upon heating, which beside the calorimetric anomalies around this temperature confirms the existence of a second structural PT in $LaTaO_4$ ceramics.

Fig. 6 shows the temperature dependence of the wavenumber, linewidth, and integrated intensity ratios for the modes marked in Fig. 5, chosen as the parameters to be studied as a function of heating/cooling temperature. The errors bars are represented considering the experimental wavenumber resolution and the uncertainty values obtained from the deconvolution. The changes in the Raman spectra associated with the structural phase transitions are clearly reflected in these parameters, and the broken lines in Fig. 6 were then used to delimit the structural phases present in $LaTaO_4$ from these results. The first broken line is around 160 °C, in which the spectrum showed a noticeable change. The temperature range in which the first structure exists is represented by the symbol I in Fig. 6, for better visualization. The temperature range for the second structure is represented by II, between 160 °C and 225 °C, from the results obtained for the wavenumbers, linewidth, and integrated intensity ratios. The temperature range represented by III corresponds to the structural phase observed around 225 °C. It is important to remember that both peaks in ε′ showed the existence of thermal hysteresis upon heating/cooling. From this result, the coexistence of structural phases cannot be neglected in the temperature range between 140–170 °C. Therefore, the Raman spectra on cooling for the $LaTaO_4$ ceramics are shown in Fig. 7. Non-polar/polar structural transition was observed around 220 °C on

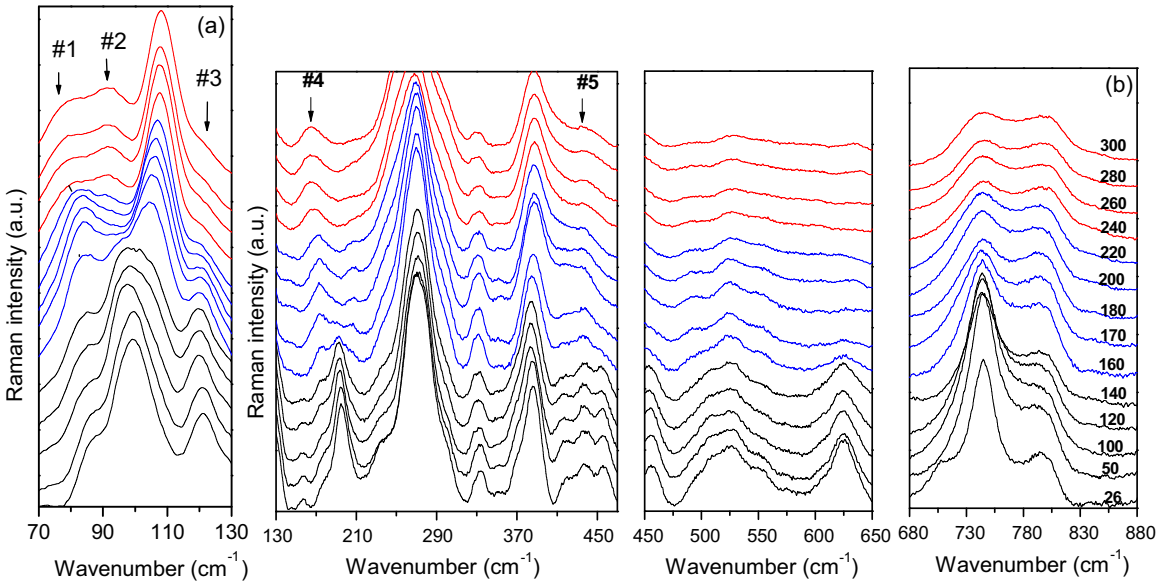

Fig. 5. Raman spectra for the $LaTaO_4$ ceramics studied upon heating: (a) 70–130 cm^{-1}; (b) 130–880 cm^{-1}. Temperatures are indicated in °C and the colors correspond to the different structural phases: black curves for the room temperature phase (monoclinic), blue curves for the intermediate (polar orthorhombic) phase, and red curves for the high temperature phase (non-polar orthorhombic). Modes marked #1 to #5 are present in all three structures (see text). (For interpretation of the references to color in this figure legend, the reader is referred to the web version of this article.)

cooling. The orthorhombic $Cmc2_1$ phase (polar) was detected practically at the same temperature than that observed on heating (Fig. 5). Also, the changes in the spectra associated with the monoclinic phase are observed below 40 °C. These results demonstrate the existence of two structural phase transitions on cooling, in good correspondence with the dielectric and calorimetric behaviors discussed previously.

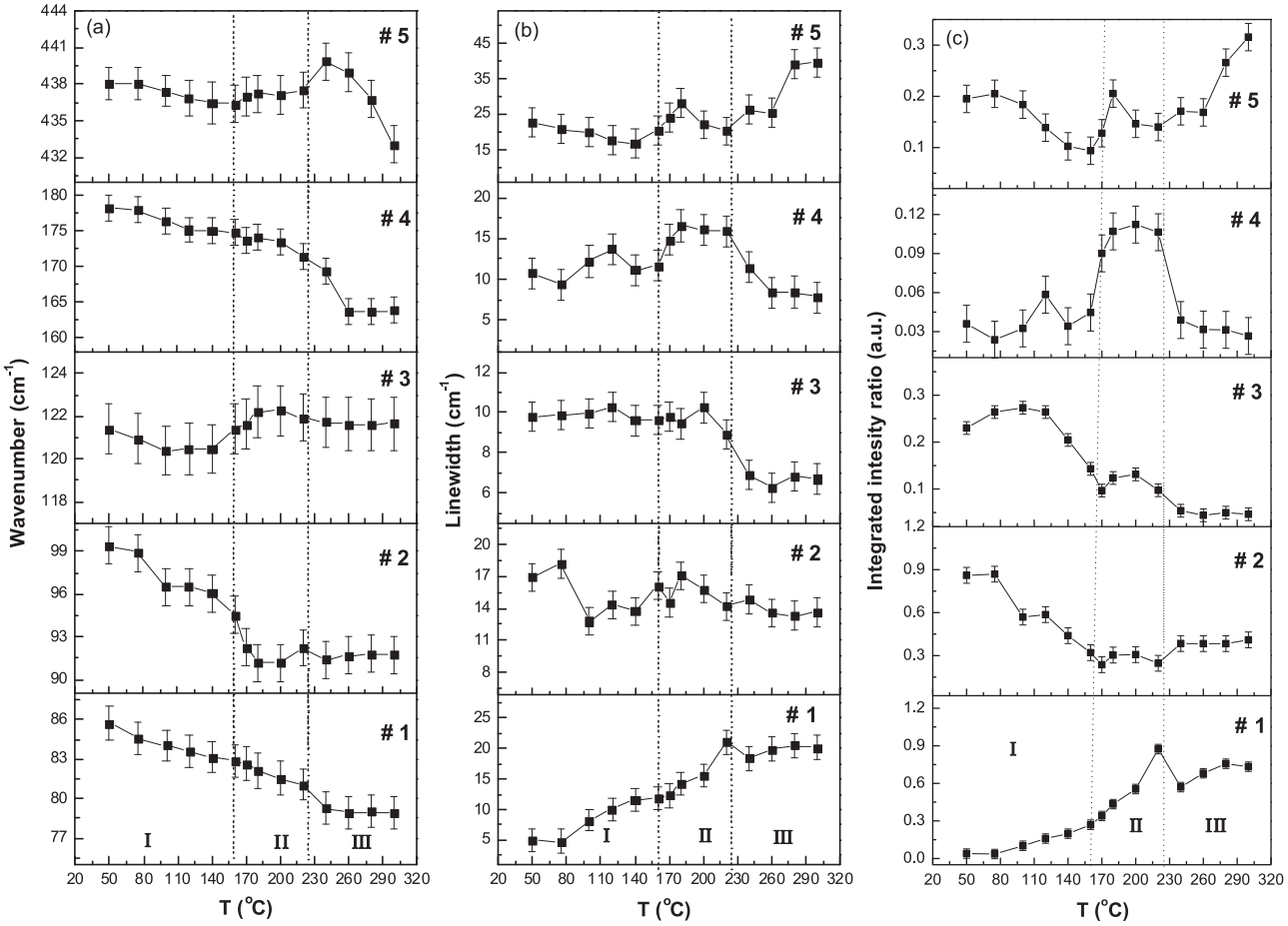

Fig. 6. Temperature dependence of the (a) wavenumber, (b) linewidth, and (c) integrated intensity ratio for the modes marked in Fig. 5. Three regions are represented by dotted curves: I (centrosymmetric monoclinic phase); II (non-centrosymmetric orthorhombic phase); and III (orthorhombic non-polar phase). Error bars are represented considering the uncertainty in the wavenumber measure and the uncertainty values obtained from the deconvolution.

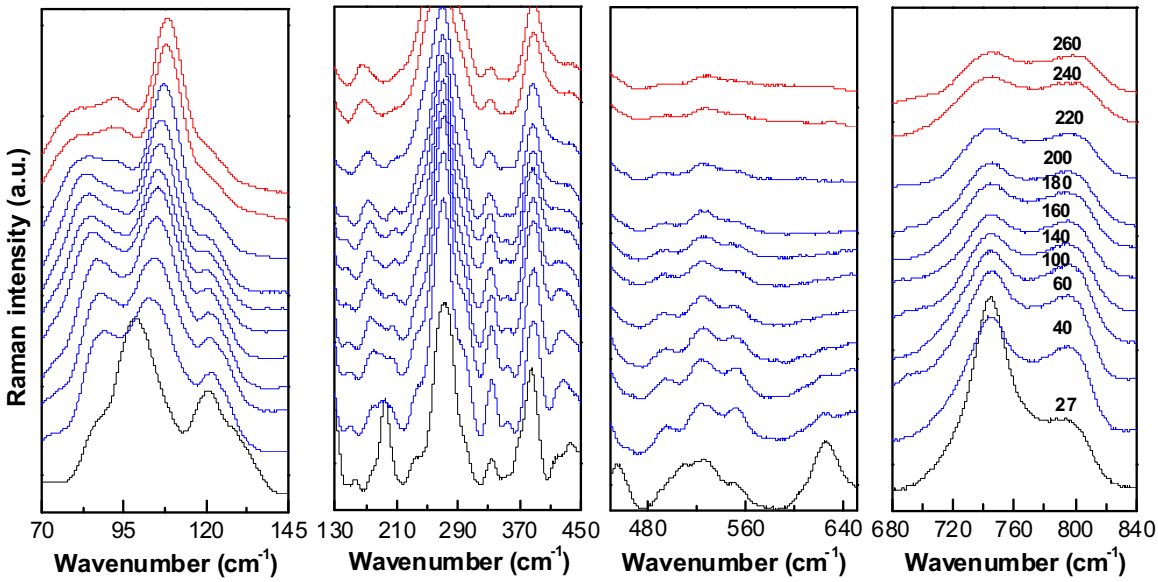

Fig. 7. Raman spectra for the $LaTaO_4$ studied sample at several temperatures (°C) upon cooling. The colors correspond to the different observed structural phases: black lines for the monoclinic phase, blue lines for the orthorhombic polar phase, and red lines for the non-polar orthorhombic phase. (For interpretation of the references to color in this figure legend, the reader is referred to the web version of this article.)

Table 1
Factor-group analysis for all crystal structures expected for $LaTaO_4$ ceramics.

Atom	Wyckoff sites	Symmetry	Irreducible representations
Phase I (AFE): Monoclinic $P2_1/c$, #14,C_{2h}^5			
La	4*e*	C_1	$3A_g+3A_u+3B_g+3B_u$
Ta	4*e*	C_1	$3A_g+3A_u+3B_g+3B_u$
O(1)	4*e*	C_1	$3A_g+3A_u+3B_g+3B_u$
O(2)	4*e*	C_1	$3A_g+3A_u+3B_g+3B_u$
O(3)	4*e*	C_1	$3A_g+3A_u+3B_g+3B_u$
O(4)	4*e*	C_1	$3A_g+3A_u+3B_g+3B_u$
$\Gamma_{TOTAL}=18A_g+18B_g+18A_u+18B_u$, $\Gamma_{ACOUSTIC}=A_u+2B_u$			
$\Gamma_{RAMAN}=18A_g+18B_g$ and $\Gamma_{INFRARED}=17A_u+16B_u$			
Phase II (FE): Orthorhombic $Cmc2_1$, #36, C_{2v}^{12}			
La	4*a*	C_s^{yz}	$2A_1+A_2+B_1+2B_2$
Ta	4*a*	C_s^{yz}	$2A_1+A_2+B_1+2B_2$
O(1)	4*a*	C_s^{yz}	$2A_1+A_2+B_1+2B_2$
O(2)	4*a*	C_s^{yz}	$2A_1+A_2+B_1+2B_2$
O(3)	4*a*	C_s^{yz}	$2A_1+A_2+B_1+2B_2$
O(4)	4*a*	C_s^{yz}	$2A_1+A_2+B_1+2B_2$
$\Gamma_{TOTAL}=12A_1+6A_2+6B_1+12B_2$, $\Gamma_{ACOUSTIC}=A_1+B_1+B_2$			
$\Gamma_{RAMAN}=11A_1+6A_2+5B_1+11B_2$ and $\Gamma_{INFRARED}=11A_1+5B_1+11B_2$			
Phase III (PE): Orthorhombic *Cmcm*, #63, D_{2h}^{17}			
La	4*a*	C_{2h}^x	$A_u+2B_{1u}+2B_{2u}+B_{3u}$
Ta	4*c*	C_{2v}^y	$A_g+B_{1g}+B_{1u}+B_{2u}+B_{3g}+B_{3u}$
O(1)	8*g*	C_s^{xy}	$2A_g+A_u+2B_{1g}+B_{1u}+B_{2g}+2B_{2u}+B_{3g}+2B_{3u}$
O(2)	8*f*	C_s^{yz}	$2A_g+A_u+B_{1g}+2B_{1u}+B_{2g}+2B_{2u}+2B_{3g}+B_{3u}$
$\Gamma_{TOTAL}=3A_u+5A_g+4B_{1g}+6B_{1u}+2B_{2g}+7B_{2u}+4B_{3g}+5B_{3u}$, $\Gamma_{SILENT}=3A_u$, $\Gamma_{ACOUSTIC}=B_{1u}+B_{2u}+B_{3u}$			
$\Gamma_{RAMAN}=5A_g+4B_{1g}+2B_{2g}+4B_{3g}$ and $\Gamma_{INFRARED}=5B_{1u}+6B_{2u}+4B_{3u}$			

In order to improve our understanding on the vibrational behavior of $LaTaO_4$, group theory calculations were carried out. Table 1 presents all relevant information required by the analyses, for the three likely structures presented by the sample: the occupied Wyckoff positions, the site symmetry and the phonons distribution at the Brillouin zone center in terms of the irreducible representations (determined from the nuclear site method developed by Rousseau et al. [19]). According to the group theory calculations presented in Table 1, there would be 36 Raman-active modes for $LaTaO_4$ ($18A_g+18B_g$) in the $P21/c$ space group (AFE phase I), besides the 33 infrared-active ($17A_u+16B_u$) [8,13]. For the polar orthorhombic $Cmc2_1$ (FE phase II), the group theory predicts 33 Raman modes ($11A_1+6A_2+5B_1+11B_2$), which include the 27 infrared-active polar modes ($11A_1+5B_1+11B_2$) [20]. The second phase transition is associated with the polar orthorhombic ($Cmc2_1$) to non-polar orthorhombic (*Cmcm*, PE phase III), where only 15 Raman modes (Table 1) are expected ($5A_g+4B_{1g}+2B_{2g}+4B_{3g}$) besides 15 infrared-active bands ($5B_{1u}+6B_{2u}+4B_{3u}$) [20-22].

Table 2 shows the Raman modes identified for each structure at room temperature, 180 °C and 240 °C, after fitting procedures by using Lorentzian curves. While the number of observed Raman bands match perfectly the group theory predictions for the high temperature structures (15 modes for phase III and 33 modes for phase II), the number of modes observed at room temperature (phase I) for $LaTaO_4$ ceramics is higher (41 bands) than that predicted by group theory for the monoclinic $P21/c$ structure (36 bands). Five additional modes were thus observed and are indicated in blue in Table 2. Fig. S1 presents

Table 2
Raman-active modes observed at room temperature (RT), 180 °C and 240 °C for $LaTaO_4$ ceramics (extra modes are in blue, see text for discussion).

Band (#)	Wavenumber (cm^{-1})			Band (#)	Wavenumber (cm^{-1})		
	RT	180 °C	240 °C		RT	180 °C	240 °C
1	57.6	52.8	79.3	22	300.4	386.8	
2	60.7	82.1	91.4	23	**327.7**	412.1	
3	86.4	85.4	107.8	24	334.5	437.0	
4	94.7	91.2	121.7	25	**369.7**	495.0	
5	99.7	96.7	165.1	26	378.8	525.1	
6	105.5	104.1	175.5	27	385.0	550.9	
7	121.7	106.3	249.6	28	391.3	744.6	
8	130.0	108.7	268.2	29	396.7	753.2	
9	**144.7**	122.2	300.1	30	419.1	769.8	
10	153.6	125.0	336.2	31	437.0	774.6	
11	157.6	174.2	388.0	32	457.7	793.7	
12	174.5	206.0	439.8	33	490.5	801.7	
13	179.9	207.9	525.9	34	507.4		
14	193.6	245.5	740.1	35	528.5		
15	199.9	260.9	803.9	36	552.6		
16	232.8	269.8		37	623.6		
17	**239.5**	287.6		38	718.0		
18	260.9	292.6		39	744.0		
19	269.6	302.5		40	791.9		
20	280.1	331.5		41	804.2		
21	**293.1**	354.0					

(Supporting Information), for the ceramics with monoclinic structure (room temperature), all the Raman-active bands identified after fitting procedures (Lorentzian curves are in green and blue curves, while the fitting curve is showed in red). The additional modes (showed in blue in Fig. S1) are believed to be infrared-active bands, which could be activated due to local distortion of the lattice associated with the presence of point defects (oxygen vacancies) with consequent weakening of the selection rules. In order to investigate this point, infrared reflectivity measurements were conducted in polished samples and the experimental spectra were adjusted within the four-parameter semi-quantum model [23], with a non-linear least-square program [24]. Within this model, the infrared phonon contribution of the N polar phonons to the complex dielectric dispersion function $\varepsilon(\omega)$, at a wavenumber ω, is given by:

$$\varepsilon(\omega) = \varepsilon_\infty \prod_{j=1}^{N} \frac{\Omega_{j,LO}^2 - \omega^2 + i\omega\gamma_{j,LO}}{\Omega_{j,TO}^2 - \omega^2 + i\omega\gamma_{j,TO}}, \quad (1)$$

where ε_∞ is the electronic polarization contribution, and $\Omega_{j,LO}(\Omega_{j,TO})$ and $\gamma_{j,LO}(\gamma_{j,TO})$ are the frequency and damping of the j-th longitudinal (transverse) optical polar modes, respectively. At low-incidence angles, the dielectric function is related to the optical reflectivity R by the Fresnel formula [23]:

$$R = \left| \frac{\sqrt{\varepsilon(\omega)} - 1}{\sqrt{\varepsilon(\omega)} + 1} \right|^2 \quad (2)$$

For our $LaTaO_4$ ceramics, the reflectivity results are displayed in Fig. 8 (top panel) as black squares, along with the adjusted curves (solid red line) obtained after fitting the experimental reflectivity data of the sample with Eqs. (1) and (2). Visual inspection shows, at least, 18 modes for the $LaTaO_4$ ceramics. The optical functions obtained from the fittings are also presented in Fig. 8 (middle and bottom panels): imaginary part of the dielectric function, Im (ε), and imaginary part of the reciprocal dielectric constant divided by ω, Im $(\varepsilon^{-1})/\omega$. The TO and LO branches of each polar mode can be determined from the poles and zeros of real part of the dielectric constant, respectively, but the phonon polar characteristics (phonon positions and widths) are more accurately determined from the peaks in Im(ε) and Im$(\varepsilon^{-1})/\omega$.

The obtained dispersion parameters for the TO and LO infrared branches for the $LaTaO_4$ ceramic are summarized in Table 3. We note

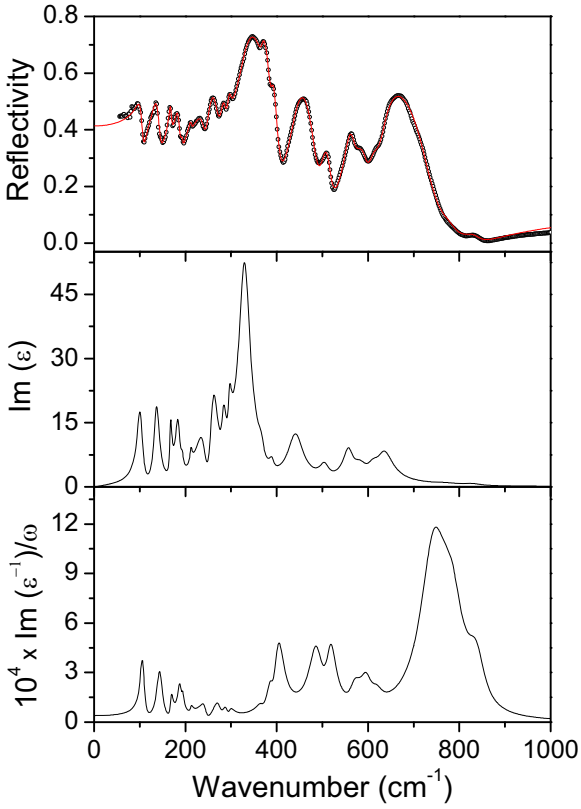

Fig. 8. Infrared experimental data and optical functions of $LaTaO_4$ ceramics. Top panel: reflectivity spectrum (black squares) and fitting curve (red solid line). Optical functions obtained from the fitting of the infrared data are showed in middle and bottom panels: imaginary part of the dielectric constant, Im(ε) (middle), and imaginary part of the reciprocal dielectric constant divided by ω to evidence the low wavenumber LO modes, Im$(\varepsilon^{-1})/\omega$ (bottom). (For interpretation of the references to color in this figure legend, the reader is referred to the web version of this article.)

Table 3
Dispersion parameters from the four parameters semi-quantum model adjust of the infrared reflectivity spectra of monoclinic $LaTaO_4$ ceramics. The wavenumbers (Ω) and damping constants (γ) are in cm^{-1}.

Band (#)	$\Omega_{j,\,TO}$	$\gamma_{j,\,TO}$	$\Omega_{j,\,LO}$	$\gamma_{j,\,LO}$
1	102.0	15.5	106.9	11.3
2	136.8	15.4	144.0	15.6
3	167.0	5.6	168.5	7.4
4	183.8	11.9	187.7	11.1
5	193.0	5.3	193.5	5.7
6	212.0	6.4	212.5	6.9
7	241.2	27.9	243.1	15.7
8	259.7	22.3	271.9	23.3
9	282.9	11.8	286.0	16.5
10	296.0	8.3	296.7	12.0
11	329.6	31.6	367.9	17.2
12	368.5	13.7	388.3	14.8
13	389.8	11.4	403.0	29.0
14	441.1	42.2	487.9	37.0
15	505.3	24.2	517.9	27.5
16	558.6	26.3	568.9	26.7
17	583.7	42.0	596.9	27.9
18	610.5	34.1	620.0	31.0
19	633.0	41.1	744.1	71.4
20	775.0	65.0	786.0	58.0
21	832.0	49.0	839.0	45.0
	ε_∞=4.63 and ε_r=21.2			

that a total of 21 infrared modes could be discerned for this sample, in reasonable accordance with the predicted modes for this monoclinic $P21/c$ structure. Indeed, for this material, the situation is quite similar

to those of $LnMgB''O_6$ (*Ln* =lanthanide; *B″*=Ti, Sn) [24–27] and Ca_2MgTeO_6 [28] compounds, where quasi-accidental degeneracy forbids the distinction between A_u and B_u modes evolving correlated vibrations, so that only 17 infrared modes are observed for those materials, instead of the 33 foreseen ones (also, $17A_u+16B_u$) [25–28]. It is worthy noticing the resemblance of the spectra of the $LaTaO_4$ and those of $LnMgB''O_6$ and Ca_2MgTeO_6, which derives from the fact that the vibrational modes come essentially from the MgO_6, $B''O_6$ and TeO_6 octahedra, as tentatively assigned in those cited references.

From the 41 bands observed in the Raman spectra at room temperature (Table 2), five were considered to be defect-activated infrared modes: 144.7, 239.5, 293.1, 327.7 and 369.7 cm^{-1}. As it can be seen in Table 3, these values are close to the TO/LO branches of the infrared active bands #2, 7, 10, 11 and 12. This result must be a consequence of the local distortion of the structure due to the presence of oxygen vacancies, which distort the monoclinic structure and thus activate infrared modes in the Raman spectra of the $LaTaO_4$ ceramics. According to group theory calculations, 36 Raman-active modes are expected for the monoclinic structure. Thus, taking into account the five defect-activated modes, our results are in perfect agreement with the predicted room temperature *P*21/c structure [8,13]. Concerning the high temperature structures, as already pointed out, the number of depicted modes observed at 180 °C and 240 °C were 33 and 15, respectively, which is also in perfect agreement with the theoretical calculations.

From the dielectric properties and from the analyses of the thermal behavior and vibrational spectroscopic data, the existence of two sequential first-order structural phase transitions in $LaTaO_4$ ceramics becomes clear. The first AFE-FE transition exhibited a very large thermal hysteresis, in the temperature range 160 °C/37 °C. The studied $LaTaO_4$ ceramics showed a surely higher monoclinic distortion than those previously observed for pure and doped $LaTaO_4$ ceramics [7,9]. This distortion seems to be related to the presence of point defects, as evidenced by the activation of infrared bands in the Raman spectra at room temperature. Moreover, this monoclinic (AFE)-to-orthorhombic (FE) transition has a reconstructive nature, once $C_{2\,h}$ is not a subgroup of C_{2v} point group (both are sub-groups of the PE D_{2h} point groups. This explains why the ferroelectric C_{2v} phase can exist in a large temperature interval and also explains partially the possible large metastability (which also depends on the presence of defects, as previously pointed out).

From the dielectric study, a high influence of the conductivity was observed on the dielectric responses, with an activation energy related with oxygen vacancies (0.62 eV). In this sense, the analogy between the $LaTaO_4$ and the isostructural $BaMnF_4$ showed that the geometrical changes on the sheets on TaO_6 octahedra produced main changes in the coordination of the lanthanum ion [7]. The geometrical modifications involve mainly the rotation of the oxygen octahedra. For the samples studied in the present work, the existence of oxygen vacancies can influence the orientation of the TaO_6 and the coordination of the lanthanum. The variation on the length of the lanthanum-oxygen bond distance could cause the additional monoclinic-orthorhombic transition observed on heating. Our results lead us to conclude that the presence of the oxygen vacancies can stabilize the monoclinic structure for the phase-pure $LaTaO_4$ ceramics. Theoretical studies support that even when the octahedral tilting drives the transition into the polar orthorhombic phase the octahedral distortion helps to stabilize the polarization in these ferroelectric materials [9]. The presence of oxygen vacancies could influence this octahedral distortion and the range of stabilization of the ferroelectric phase.

4. Conclusions

Dielectric properties, thermal analysis and vibrational spectroscopic data were investigated for $LaTaO_4$ ceramics upon heating and cooling cycles. The samples exhibited sequential first-order phase transitions upon heating from the monoclinic structure (*P*21/c) to the polar orthorhombic one ($Cmc2_1$) above 160 °C, followed by an additional phase transition to the orthorhombic *Cmcm* space group around 225 °C. Raman scattering upon heating/cooling corroborated the existence of a large thermal hysteresis observed in the real part of the dielectric permittivity for the AFE-FE (160 °C/37 °C) transition. Infrared reflectivity allows us to discern forbidden modes that were activated in the Raman spectra due to structural distortion at room temperature. The presence of this monoclinic distortion was probably caused by oxygen vacancies that can stabilize this structure and affect both octahedra distortion and lanthanum coordination. These results can explain the thermal hysteresis observed during heating/cooling cycles in the dielectric permittivity.

Acknowledgements

The authors acknowledge the financial support from CAPES, Brazil, CNPq, Brazil, FINEP, Brazil, and FAPEMIG, Brazil. Special recognition is due to Latin-American Network of Ferroelectric Materials (NET-43) by the partial funding of one of the authors (Y. G. Abreu). Thanks are also due to Prof. Glaura Goulart Silva and Felipe Luiz Queiroz Ferreira (UFMG) for the DSC measurements.

Appendix A. Supplementary material

Supplementary data associated with this article can be found in the online version at http://dx.doi.org/10.1016/j.ceramint.2016.10.128.

References

[1] R. Haugsrud, T. Norby, Proton conduction in rare-earth ortho-niobates and ortho-tantalates, Nat. Mater. 5 (2006) 193–196.
[2] T.Z. Forbes, M. Nyman, M.A. Rodriguez, A. Navrotsky, The energetics of lanthanum tantalate materials, J. Solid State Chem. 183 (2010) 2516–2521.
[3] M. Machida, S. Murakami, T. Kijima, S. Matsushima, M. Arai, Photocatalytic property and electronic structure of lanthanide tantalates, $LnTaO_4$ (Ln= La, Ce, Pr, Nd, and Sm), J. Phys. Chem. B 105 (2001) 3289–3294.
[4] F.E. Osterloh, Inorganic materials as catalysts for photochemical splitting of water, Chem. Mater. 20 (2008) 35–54.
[5] A. Hristea, E.J. Popovici, L. Muresan, M. Stefan, R. Grecu, A. Johansson, M. Boman, Morpho-structural and luminescent investigations of niobium activated yttrium tantalate powders, J. Alloy. Compd. 471 (2009) 524–529.
[6] X. Xiao, B. Yan, $REMO_4$ (RE= Y, Gd; M= Nb, Ta) phosphors from hybrid precursors: microstructure and luminescence, J. Mater. Res. 23 (2008) 679–687.
[7] R.J. Cava, R.S. Roth, The structure of $LaTaO_4$ at 300°C by neutron powder profile analysis, J. Solid State Chem. 36 (1981) 139–147.
[8] K.P. Siqueira, G.B. Carvalho, A. Dias, Influence of the processing conditions and chemical environment on the crystal structures and phonon modes of lanthanide orthotantalates, Dalton Trans. 40 (2011) 9454–9460.
[9] K.J. Cordrey, M. Stanczyk, C.A. Dixon, K.S. Knight, J. Gardner, F.D. Morrison, P. Lightfoot, Structural and dielectric studies of the phase behaviour of the topological ferroelectric $La_{1-x}Nd_xTaO_4$, Dalton Trans. 44 (2015) 10673–10680.
[10] M. Nyman, M.A. Rodriguez, L.E. Rohwer, J.E. Martin, M. Waller, F.E. Osterloh, Unique $LaTaO_4$ polymorph for multiple energy applications, Chem. Mater. 21 (2009) 4731–4737.
[11] J.F. Scott, Searching for new ferroelectrics and multiferroics: a user's point of view. npj Computational, Materials 1 (2015) 15006.
[12] F. Vullum, F. Nitsche, S.M. Selbach, T. Grande, Solid solubility and phase transitions in the system $LaNb_{1-x}Ta_xO_4$, J. Solid State Chem. 181 (2008) 2580–2585.
[13] K.P. Siqueira, A. Dias, Effect of the processing parameters on the crystalline structure of lanthanide orthotantalates, Mater. Res. 17 (2014) 167–173.
[14] N.G. Teixeira, R.L. Moreira, M.R.B. Andreeta, A.C. Hernandes, A. Dias, Micro Far-Infrared Reflectivity of $CaNb_2O_6$ Single Crystal Fibers Grown by the Laser-Heated Pedestal Growth Technique, Cryst. Growth Des. 11 (2011) 3472–3478.
[15] R.L. Moreira, R.M. Almeida, K.P. Siqueira, C.G. Abreu, A. Dias, Optical phonon modes and infrared dielectric properties of monoclinic $CoWO_4$ microcrystals, J. Phys. D: Appl. Phys. 49 (2015) 045305.
[16] T. Lu, B.C.H. Steele, Electrical conductivity of polycrystalline $BiVO_4$ samples having the scheelite structure, Solid State Ion. 21 (1986) 339–342.
[17] H. Fjeld, K. Toyoura, R. Haugsrud, T. Norby, Proton mobility through a second order phase transition: theoretical and experimental study of $LaNbO_4$, Phys. Chem. Chem. Phys. 12 (2010) 10313–10319.
[18] G. Gasparotto, N.M. Nascimento, M.A. Cebim, J.A. Varela, M.A. Zaghete, Effect of heat treatment on the generation of structural defects in $LaTaO_4$ ceramics and their correlation with photoluminescent properties, J. Alloy. Compd. 509 (2011)

9076–9078.
[19] D.L. Rousseau, R.P. Bauman, S.P.S. Porto, Normal mode determination in crystals, J. Raman Spectrosc. 10 (1981) 253–290.
[20] A.F. Murray, G. Brims, S. Sprunt, Deviations from soft mode behaviour in the Raman spectrum of incommensurate $BaMnF_4$, Solid State Commun. 39 (1981) 941–946.
[21] D. Errandonea, O. Gomis, B. García-Domene, J. Pellicer-Porres, V. Katari, S.N. Achary, A.K. Tyagi, C. Popescu, New Polymorph of $InVO_4$: a High-Pressure Structure with Six-Coordinated Vanadium, Inorg. Chem. 52 (2013) 12790–12798.
[22] E.J. Baran, M.E. Escobar, The vibrational spectra of $InVO_4$ and $TlVO_4$, Spectrochim. Acta A 41 (1985) 415–417.
[23] F. Gervais, P. Echegut, Incommensurate Phases in Dielectrics, North Holland, Amsterdam, 1986.
[24] D.D.S. Meneses, G. Gruener, M. Malki, P. Echegut, Causal Voigt profile for modeling reflectivity spectra of glasses, J. Non-Cryst. Solids 351 (2005) 124–129.
[25] A.N. Salak, D.D. Khalyavin, V.M. Ferreira, J.L. Ribeiro, L.G. Vieira, Structure refinement, far infrared spectroscopy, and dielectric characterization of (1–x) $La(Mg_{1/2}Ti_{1/2})O_3$–$xLa_{2/3}TiO_3$ solid solutions, J. Appl. Phys. 99 (2006) 094104.
[26] G.S. Babu, V. Subramanian, V. Murthy, I.N. Lin, C.T. Chia, H.L. Liu, Far-infrared, Raman spectroscopy, and microwave dielectric properties of $La(Mg_{0.5}Ti_{(0.5-x)}Sn_x)O_3$ ceramics, J. Appl. Phys. 102 (2007) 064906.
[27] G.S. Babu, V. Subramanian, V.R.K. Murthy, R.L. Moreira, R.P.S.M. Lobo, Crystal structure, Raman spectroscopy, far-infrared, and microwave dielectric properties of $(1-x)La(MgSn)_{0.5}O_3$–$xNd(MgSn)_{0.5}O_3$ system, J. Appl. Phys. 103 (2008) 084104.
[28] A. Dias, G. Subodh, M.T. Sebastian, M.M. Lage, R.L. Moreira, Vibrational studies and microwave dielectric properties of A-site-substituted tellurium-based double perovskites, Chem. Mater. 20 (2008) 4347–4355.